Journal of Volcanology and Geothermal Research 471 (2026) 108536

Contents lists available at ScienceDirect

Journal of Volcanology and Geothermal Research

journal homepage: www.journals.elsevier.com/journal-of-volcanology-and-geothermal-research

Investigating the seismic structure of shallow magmatic conduits: Insights from the Salina Island (southern Italy)

I. Granados-Chavarría [a,*], F. Di Luccio [a,*], M. Calò [b], D. Famiani [a], M. Lupi [c], M. Palano [d,e], G. Ventura [a,f]

[a] Istituto Nazionale di Geofisica e Vulcanologia, Rome, Italy
[b] Instituto de Geofísica, UNAM, Mexico City, Mexico
[c] Department of Earth Sciences, University of Geneva, Geneva, Switzerland
[d] University of Palermo, Palermo, Italy
[e] Istituto Nazionale di Geofisica e Vulcanologia, Catania, Italy
[f] Istituto di Scienze Marine, Consiglio Nazionale delle Ricerche, Napoli, Italy

A R T I C L E I N F O

Keywords:
Nodal array
Plumbing system
Ambient noise tomography

A B S T R A C T

The plumbing systems of closely spaced individual volcanoes and volcanic fields may be very complex due to the interaction (or not) of different magma storage zones and magma pathways at variable depths. Ambient noise tomography unveils the shallow seismic structure of Salina Island (Southern Italy), which is characterized by 6 proximal and partly overlapping volcanoes developed between 244 and 15.6 ka. We use two months of continuous data from 40 nodal stations deployed in 2023 at uneven interstation distances. This seismic array yields tomographic maps down to 1.5 km depth in which the geometry of the volcano flank collapses and shallower plumbing systems of eruptive fissures are clearly imaged. Shear wave velocity maps reveal the main structures and deposits of the 'twin' stratovolcanoes of Monte dei Porri, to the west, and Monte Fossa delle Felci, to the east. High velocity anomalies beneath these volcanoes become less pronounced at ~200 m b.s.l. revealing the transition from submarine to subaerial lava flows. 3D images of the eastward dipping subcircular conduits below the main volcanoes suggest that the deep feeding system is located offshore to the east.

1. Introduction

The spatial distribution of volcanoes is mainly governed by large scale geodynamic processes while local tectonics controls the location of individual, proximal volcanoes and volcanic fields. These latter are constituted by a group of spatially closed monogenetic and/or polygenetic edifices including purely monogenetic cones and stratovolcanoes (Canón-Tapia, 2016). The plumbing systems of volcanic fields or proximal volcanoes may be very complex due to tectonic processes, magma production rate in the mantle and accumulation in the crust, crustal rheological layering (Annen et al., 2025; Li et al., 2021). In some cases, the plumbing systems of closely spaced volcanoes may interact as in the case of 30 km apart Mauna Loa and Kīlauea volcanoes, which were characterized by an anticorrelated eruptive behavior (Klein, 1982) in the way that inflation of a reservoir modulates the volcanic activity on the other volcano by stress changes (Przeor et al., 2022). A similar interaction has been suggested for Eyjafjallajökull (Iceland), as detailed by Albino and Sigmundsson (2014). Also, the 10 km spaced Irazú and Turrialba volcanoes (Costa Rica) have a common plumbing system at 10–15 km depth and separated, shallower magma storage zones (DeVitre et al., 2019). Results from geodetic measurements and ambient noise tomography (Muller et al., 2024; Jiwani-Brown et al., 2022) show that inflation beneath Irazú may trigger eruptions at either Irazú or Turrialba. Conversely, the crustal plumbing systems of Avacha and Koryaksky twin stratovolcanoes in Kamchatka appear unconnected (Bushenkova et al., 2019). These reported examples show that the plumbing system(s) and shallow conduits of volcanoes in near proximity, twin volcanoes, and volcanic fields may interact (or not) in different ways. Therefore, the knowledge of the geometry and size of the magma storage zones and shallow magma pathways is of primary importance not only for the volcanic hazard implications but also to study the inner structure of volcanoes and underneath shallow crust. While information on the intracrustal and mantle magma storage zones below volcanoes are relatively well known (Abe et al., 2017; Bedrosian

* Corresponding authors at: Istituto Nazionale di Geofisica e Vulcanologia, via di Vigna Murata 605, Rome, Italy.
E-mail addresses: ivan.granadoschavarria@ingv.it (I. Granados-Chavarría), francesca.diluccio@ingv.it (F. Di Luccio).

https://doi.org/10.1016/j.jvolgeores.2026.108536
Received 13 August 2025; Received in revised form 6 January 2026; Accepted 15 January 2026
Available online 19 January 2026
0377-0273/

et al., 2018; Heath et al., 2019; McVey et al., 2020; Chambers et al., 2021; Paulatto et al., 2022), the shallower magma pathways, e.g. conduits and dikes, are not fully understood. This is particularly true in volcanic fields, where closely spaced volcanoes may be characterized by potentially crosscutting circular to dike-like conduits (Canón-Tapia, 2016; Smith and Németh, 2017; Albert et al., 2025). In addition, interactions with the uppermost layers of the crust may also control the distribution of vents.

Seismic tomography is a crucial approach for investigating active volcanoes (Patanè et al., 2006; Agius et al., 2022; Totaro et al., 2022) and even for geothermal exploration (Cabrera-Pérez et al., 2023), since it provides a valuable image of the mechanical properties of volcanic edifices, laterally and in depth, to better understand its inner structure. Ambient Noise Tomography (ANT) has been widely recognized as an effective method for imaging the seismic structure of the shallow crust using ambient seismic noise (Esquivel-Mendiola et al., 2024), particularly in areas with sparse or absent seismicity where classic approaches as arrival time tomography would be challenging. ANT has been applied on a wide range of volcanoes, from active (De Siena et al., 2018; Granados-Chavarría et al., 2022; Cabrera-Pérez et al., 2023; Spica et al., 2017; Stumpp et al., 2025) to quiescent edifices (Calò et al., 2023).

ANT is based on the diffuse field theory (Bensen et al., 2007, and references therein) and aims to calculate the Empirical Green's Functions (EGF) from the cross-correlation functions of the continuous ambient noise waveforms between station-pairs, the longer the duration of the continuous records the better the quality of the retrieved GF (Shapiro and Campillo, 2004). From each GF, it is possible to extract the surface waves dispersion curves (group and phase velocity) through a frequency-time analysis (FTAN) and then calculate the shear-wave velocity model at depth. A key advantage of this technique is that its resolution improves with an increasing number of seismic stations. To this regard, the introduction of seismic nodes, as autonomous, cable-free, easy-to-install seismic sensors, smaller than traditional seismometers, has allowed the quick deployment of dense seismic networks, especially in volcanic settings where topography can be an issue.

The Aeolian Archipelago consists of seven volcanic islands and minor seamounts located in the southern Tyrrhenian Sea (southern Italy), where the subduction of the oceanic Ionian plate below the continental Calabrian arc occurs (Fig. 1a). Our study unveils the first 3D shear-wave velocity model of Salina, the northernmost island of the central volcanic

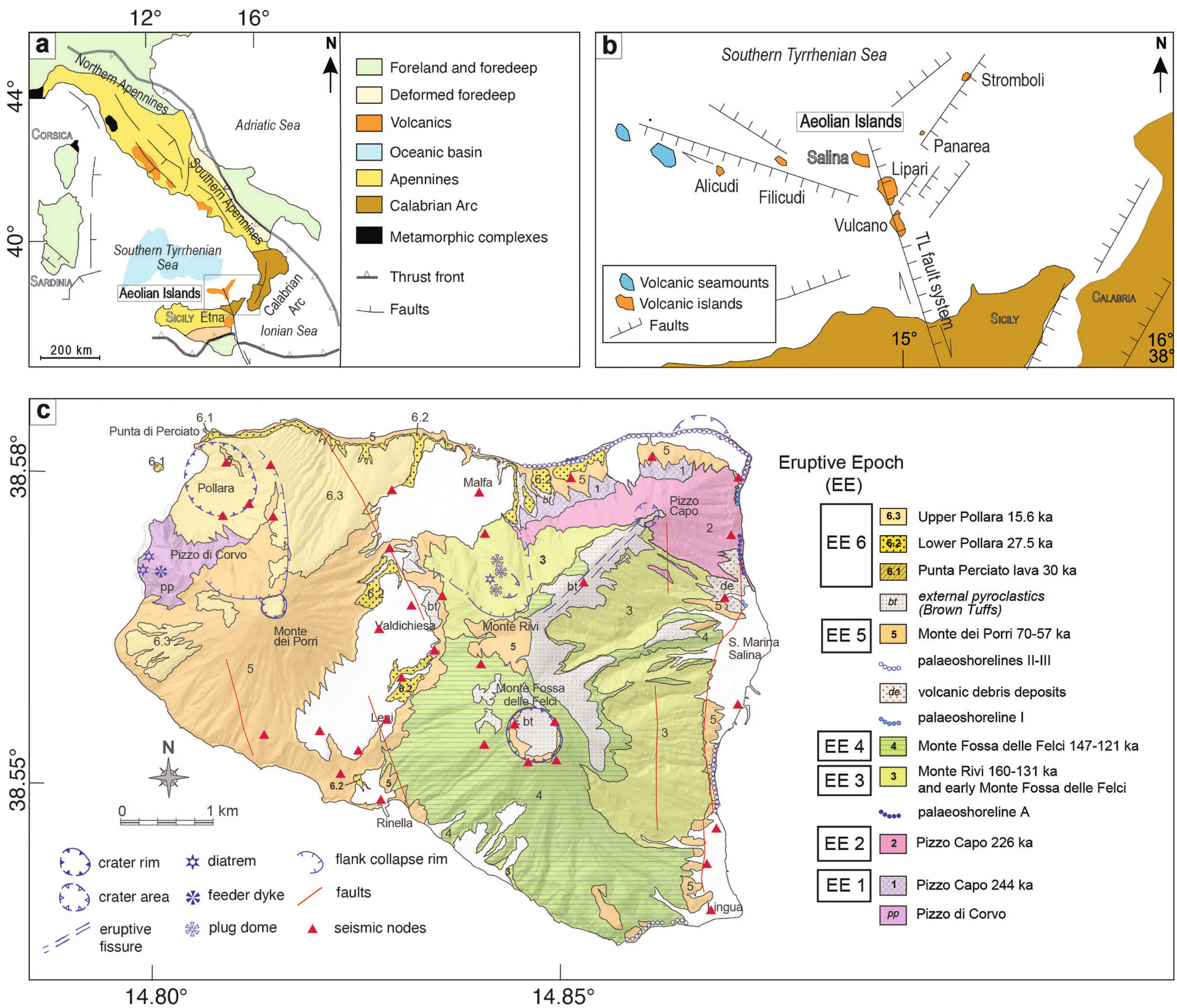

Fig. 1. Geological map of the study region (modified after Lucchi et al., 2013). In **a)** the main tectonic structure of Italy is shown. **b)** The main fault systems of the southern Tyrrhenian Sea are displayed. **c)** The Salina Island geological and volcanic features are outlined along with the eruptive epochs.

ridge, using two-months of continuous seismic data recorded by a nodal seismic network distributed in the island. In about 25 km^2, Salina hosts two main 'twin' stratovolcanoes, an eruptive fissure zone, a tuff-ring, and two older, partly eroded and collapsed volcanoes. In addition, the island represents the top of mainly submerged volcanic structures some of which characterized by a coeval activity. Therefore, Salina represents an ideal laboratory to study the interactions between shallow plumbing systems and conduit interactions at volcanic fields.

2. Geological setting

Salina is the north-westernmost island of the Vulcano-Lipari-Salina volcanic complex (Aeolian archipelago, southern Italy) emplaced along the Aeolian-Tindari-Letojanni (ATL) strike-slip fault system, a NNW-SSE striking lithospheric fault, belonging to a complex step-fault system bounding the western side of the northwest Ionian slab rolling-back below the Calabrian Arc (Fig. 1b; Billi et al., 2022; De Astis et al., 2003; Rosenbaum and Lister, 2004). The Sisifo-Alicudi (SA) fault system, a WNW-ESE oriented strike-slip shear zone, represents the easternmost tectonic lineament extending from Salina-Lipari-Vulcano complex westward (Fig. 1b; Finetti and Del Ben, 1986; Bortoluzzi et al., 2010). The southern sector of the volcanic complex is characterized by pull-apart type structures, defined by the interplay of the major strike-slip shear zones and secondary-order N-S to NNE-SSW trending normal faults (e.g. Ventura et al., 1999; Lucchi et al., 2013). Geological and geophysical data indicates that ATL guides magma uprising to the surface (De Astis et al., 2003). Crustal seismicity in the Tyrrhenian Sea clusters along the ATL and SA fault systems with the largest events occurred in 1978 (M5.6) and 1980 (M5.7) on ATL and SA, respectively (Neri et al., 1996).

The Salina Island is characterized by the 'twin' cone-shaped stratovolcanoes of Monte Fossa delle Felci (MtFF) to the east and Monte dei Porri (MtP) to the west, both rising about 2000 m from the seafloor reaching an altitude of 962 m and 830 m a.s.l., respectively (Fig. 1c). The island also includes the partly dismantled and collapsed Pizzo di Corvo (PCo), Pizzo Capo (PCa) and Monte Rivi (MtR) edifices (Keller, 1980; Lucchi et al., 2013). Salina volcanism includes early basaltic fissure eruptions and dykes, followed by more evolved products from the 'twin' central volcanoes and Pollara tuff-ring (Lucchi et al., 2013). Volcanism started at about ∼244 ka and can be divided into six main eruptive epochs (EEs), with magmas varying in composition from calc-alkaline and HK calcalkaline basalts to later rhyolites (Lucchi et al., 2013). The oldest products are basaltic lavas and scoriae erupted by the NE-SW elongated PCa fissure (EE1–2; 244–226 ka), and MtR (EE3; 160–131 ka), whose southern portion is overlapped by the northern flank of the MtFF suggesting a close spatial relationship between the shallow plumbing systems of MtR and MtFF. The MtFF activity developed between 160 and 121 ka (EE3–4), whereas the MtP stratovolcano erupted between 70 and 57 ka (EE5). MtFF and MtP emitted basaltic-andesitic to andesitic lava flows and scoriae (Fig. 1c). The MtP northwestern flank is affected by flank collapse within which the Pollara crater develops (EE6) and hosts the Punta Perciato andesitic lava flows (30 ka) and rhyolitic pumices of two subplinian eruptions (27.5 and 15.6 ka). The last significant volcanic activity on Salina occurred at ca. 15 ka forming the Pollara crater (Lucchi et al., 2013), in the north-westernmost corner of the island (Fig. 1c); this discontinuous volcanic activity reflects quiescence periods that may last from 27 to 12 ka. Magnetic data (Cocchi et al., 2019) show that the structure of Salina consists of early dykes later ($<$ 160 ka) coalescing and forming magma reservoirs from which sub-vertical, circular conduits upraise to the surface. Salina's faults show prevalent NW-SE to N-S strikes and cut MtP and the eastern MtFF flank. As mentioned above, these faults represent second-order structures of the ATL main fault system (Lucchi et al., 2013). The emission of thermal waters and hydrothermal activity have been well documented both onshore (eastern and northern onshore of Salina, Italiano and Caruso, 2011) and offshore (eastward by the coastal belt; Romagnoli et al., 1989; Madonia et al., 2022). In the framework of long quiescent periods characterizing the Salina volcanism, this feature, coupled with the occurrence of a low energetic level and persistent crustal seismicity indicates that the volcano is likely in a quiescent stage and a future reactivation of the magmatic system cannot be excluded.

3. Data and methodology

We deployed a dense seismic array in Salina Island from 21 October to 26 December 2023. The array was composed of 24 SmartSolo IGU-16HR three-component seismic nodes (5 Hz), and 16 GS-One three-component nodes (10 Hz) coupled with 16 Geospace GSB-3 digitizers. The geometry of the array, ruled by the topography of the island, is shown in Fig. 1c, and interstation distance range between 400 m and 7 km. Data was acquired in continuous mode at 250 samples per second.

To perform ANT, we retrieved the cross-correlation functions of the vertical components of the signals following the standard procedure of Bensen et al. (2007) and modified by Granados-Chavarría et al. (2022). Pre-processing of the input data included down-sampling of the signals to 40 sps, bandpass filtering from 0.15 to 6 Hz, and the temporal (1 bit) and spectral (whitening) normalization. Cross-correlation functions were calculated on synchronized 5-min-long time windows with 50% overlapping for the entire continuous records (almost two months) for each station-pair, an example is shown in the supplementary material (Fig. S1).

Each Green's Function (GF) was computed to obtain the group velocity dispersion curves via frequency-time analysis (FTAN) using the Noisy Dispersion Curve Picking program (Granados-Chavarría et al., 2019) for the anticausal and causal components. To identify the stacking method yielding GFs with the highest signal-to-noise ratio and the clearest dispersion curves, we tested the common linear stacking approach and the Phase Weighted Stacking procedure (PWS, Schimmel, M., 1999). FTAN was applied to the resulting correlograms as a diagnostic tool to compare the performance of the stacking methods. We observed that the common linear stacking approach provided the best coherency in the retrieved Rayleigh waves, in both causal and anticausal parts along the whole distance range. A detailed description of this analysis is shown in supplementary material (Text S1 and Fig. S2). The retrieved Green's functions are shown in Fig. 2, where Rayleigh waves are clearly observed in both anticausal and causal parts.

To compute the velocity between each station-pair, we considered the distance along the relief instead of the great-circle distance, due the abrupt topographic gradients of Salina. A total of 616 dispersion curves were retrieved in the frequency range of 0.25 to 4 Hz, with group velocities varying between 0.3 and 2 km/s (Fig. 2b and c). The total ray-paths distribution maps at different frequencies are shown in supplementary material (Fig. S3).

The construction of the shear-wave velocity model was performed through a two-steps inversion of the dispersion curves, after gridding the study area in cells of different size, from 250 m × 250 m to 500 m × 500 m. We first computed the 2D group-velocity distribution maps at each frequency (tomograms), and then we inverted group velocities in each cell to obtain a 1D shear wave velocity (Vs) models at depth using a finite-element approach (Haney and Tsai, 2017).

For the calculation of the tomograms, we followed the procedure proposed by Barmin et al. (2001) for regularization, using smoothing and damping parameters optimized at each frequency by using L-curve tests (Menke, 1989; Hansen, 2001) (supplementary material, Fig. S5a). From the handpicked dispersion curves, at each frequency we selected group velocities for each station-pair at distances of at least two-wavelengths and with a velocity within ±2 standard deviations from the mean group velocity. Since the path-coverage over the study area varies at different sampled frequencies, the cell-size of the processing grids for the 2D inversions was also fitted during the checkerboard resolution test (Fig. 3). Some regions, such as the western flank of MtP and the southern region of MtFF, show poor resolution due to the scant

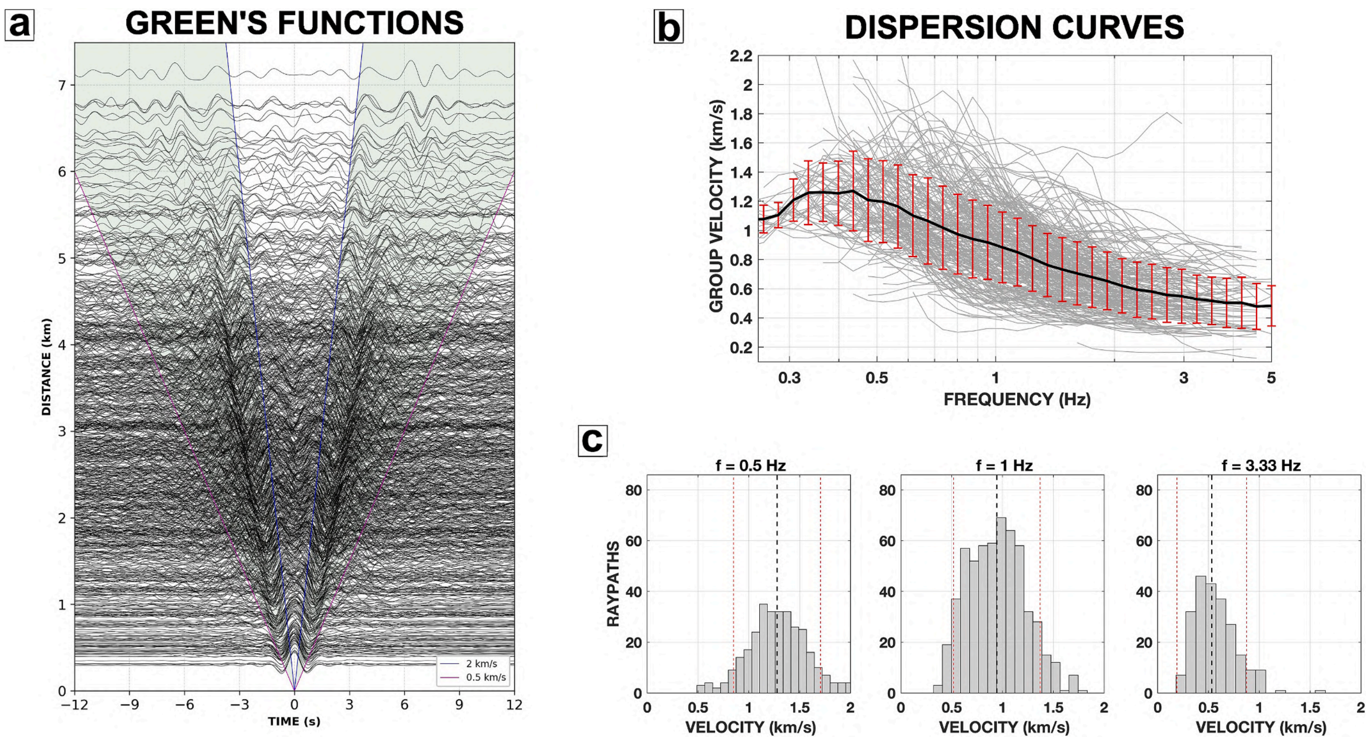

Fig. 2. Green's functions and dispersion curves. **a)** Retrieved Green's functions for all station-pairs filtered between 0.2 and 1 Hz. Colored lines correspond to velocities 0.5 km/s (magenta) and 2 km/s (blue), respectively. **b)** All group velocity dispersion curves (gray lines) and the corresponding mean dispersion curve (black thick line) and standard deviation (red bars). **c)** Histograms of the retrieved group velocity dispersion curves at 0.5, 1 and 3.3 Hz (dashed lines correspond to the mean and standard deviation, in black and red respectively). (For interpretation of the references to colour in this figure legend, the reader is referred to the web version of this article.)

raypath density, as also shown by the standard checkerboard (Fig. 3) and the spike-model (Rawlinson and Spakman, 2016; Figs. S3 and S4) resolution tests.

To overcome the recovery level of each single tomogram, we performed a post-processing step like the Weighted Average Model (WAM) technique proposed by Calò et al. (2013) for travel time tomography and described in supplementary material (Text S2 and Fig. S5). Resulting tomograms were resampled into a 250 m × 250 m cell-size grid to construct new group velocity dispersion curves (supplementary material, Fig. S6).

Finally, we inverted each dispersion curve to obtain a 1D Vs model in each cell using a perturbational approach (Haney and Tsai, 2017). As an initial model for the inversion, we tested different homogeneous models in each cell, and then we used the obtained final four layers model to invert for all cells. During the inversion, the calculated sensitivity kernels show that a reliable depth resolution can be achieved down to 1.2–1.5 km of depth (supplementary material, Fig. S7). To construct the final 3D Vs model, we gathered all 1D Vs models into a regular meshgrid in which the topography of the island is included at top of each 1D shear wave velocity model.

4. Results

The 3D shear wave velocities of Salina are shown in mapview in Fig. 4 (panels a-d) at different depths and in cross-sections (panels e-i) as velocity anomalies, along with the resolution contours. Slices and profiles of absolute Vs are shown in the supplementary material (Figs. S8, S9 and S10), as well as the depth resolution tests (supplementary material, Text S3 and Fig. S11).

Tomographic images identify an overall low velocity in the first 400–600 m b.s.l. beneath the coastline and in the central region (Fig. 4 and Fig. S8). The low shear wave velocities overlap pyroclastic and recent alluvium/colluvium beach deposits (Fig. 1) from 100 m a.s.l. to 100 m depth (Fig. 4a and b). Low velocity L1 is centered at the Pollara depression, NW of MtP (Fig. 1c for locations), where a strong gradient rules the topography, whereas L2 is between MtP and MtFF and laterally extends for ~2 km at 100 m b.s.l. (Fig. 4a and b). At 100 m b.s.l., Vs reaches 1.7 km/s below the topography highs of MtP, MtFF, and PCa that are labeled in Fig. 4a and b as H1, H2 and H3, respectively. At 400 m b.s.l., low velocity L3 is well evident from the NE flank of MtFF southeastward (Fig. 4c and g), whereas high velocities H1 below MtP, H2 beneath MtFF and H3 below PCa laterally extend and the new well-focused high velocity body H4 takes shape in north-central Salina. In Fig. 4d, at 1000 m b.s.l. the mean velocity is ~1.7 km/s, although H1 and H2 are still separated by a smooth low velocity zone that is much wider than at shallower depths.

In Fig. 4, the W-E (A-A', panel e), three S—N profiles (panels f, h, i) and the NW-SE (B-B′, panel g, crossing the volcanic fissure zone) show the lateral extension of the main features of the 3D shear wave velocity model in terms of velocity anomalies (ΔVs) to highlight velocity changes with respect to a 1D average model (supplementary material, Fig. S7e). Profile A-A' depicts the two anomalies H1 and H2 below MtP and MtR, laterally extending for 2 and 3 km between 400 m a.s.l. to 400 m b.s.l., respectively, as also evidenced in Fig. 4f (H1). The high velocity anomaly H2 in Fig. 4i is imaged beneath MtFF from 800 m a.s.l. down to 400 m b.s.l. and clearly shows the common root of MtFF and MtR. Along the same A-A' transect, forward magnetic modelling (Cocchi et al., 2019; magenta line in Fig. 4e) indicates that the main crustal basement is characterized by low magnetization from W to E. The S—N westernmost profile crosscutting MtP shows that the high velocity anomaly H1 reaches ~1 km depth, whereas the thick low velocity anomaly L2 is nested in the southern flank of MtP between the sea level and 250 m depth (Fig. 4f). L2 extends southward as shown in Fig. 4h, in which the narrow (~600 m width) and horizontal H4 anomaly is evident from 150 to 550 m b.s.l. beneath the northernmost sector of Salina.

The H3 anomaly in Fig. 4g extends from the top of the eruptive

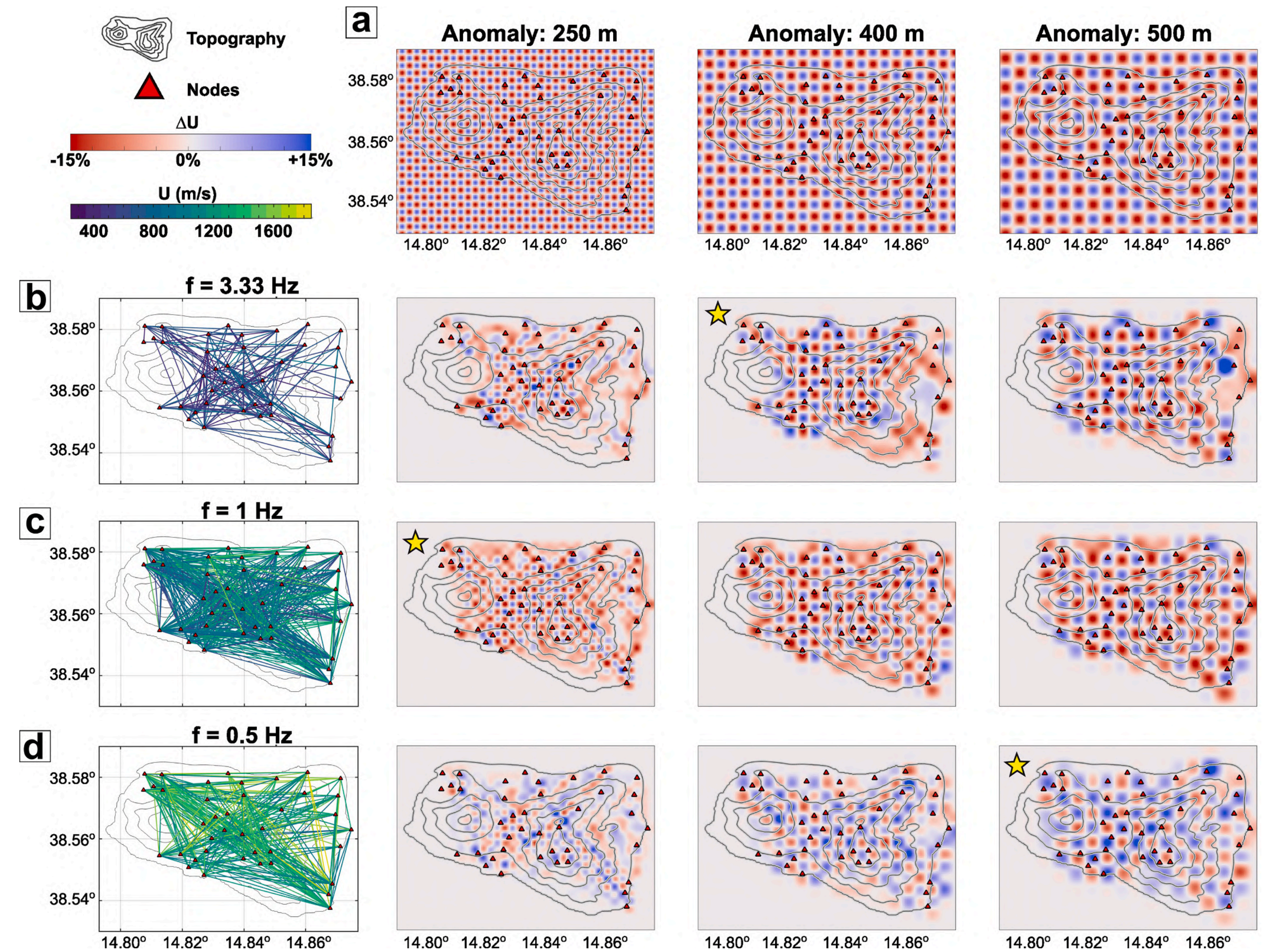

Fig. 3. Examples of resolution tests to optimize the cell-size of the corresponding processing grids at different frequencies (based on raypaths density). **a)** Checkerboard tests for different sizes of the anomalies, with each velocity anomaly corresponding to ±15% of the mean velocity at each frequency. **b, c, d)** Raypaths sampled at 3.33, 1 and 0.5 Hz from the dispersion curves, and the corresponding inverted models for each of the three different anomaly models, selected cell-size grid for each frequency is marked with a yellow star. (For interpretation of the references to colour in this figure legend, the reader is referred to the web version of this article.)

fissure (NE-SW brown line in Fig. 4a corresponding to the dashed line in Fig. 1c, in NE Salina) to ~400 m b.s.l. and deepens to the NNE as shown in profile G'-K of Fig. 5b.

In Fig. 5 we plot the geological cross-sections from Lucchi et al. (2013) overlaying a profile that crosses the 'twin' volcanoes from the western to the south-eastern coast (G-H, Fig. 5a) and a SW-NE profile extending from MtFF to PCa (profile G'-K in Fig. 5b). In Fig. 5a, at the Pollara depression (PD in Fig. 4d for location) we identify the marked low velocity anomaly L1 extending from the surface to ~500 m b.s.l. and becoming smoother at larger depths. From Pollara to the east, H1 takes place beneath MtP, whereas below Valdichiesa (Fig. 1c for location) the ~200 m thick low velocity anomaly L2 marks the depression between MtP and MtFF. H2 anomaly (+15% contour) beneath MtFF extends to the south-eastern coast of Salina (Fig. 5a), although remains shallower than H3 beneath the PCa volcanic edifice to the NE that goes deeper into the crust (Fig. 5b).

5. Discussion

Our tomographic maps and profiles shown in Figs. 4 and 5 display the main characteristics of the seismic structure from the topographic highs of Monte dei Porri and 278 Monte Fossa delle Felci (MtP and MtFF in Fig. 4d) to ~1500 m b.s.l. There is a clear correspondence between the main fault systems (brown lines in Fig. 4 a-d) and the low velocity zones. The NW-SE trending faults in the northeastern flank of MtP mark the separation between the high velocity anomalies H1 and H4, as well as H3 and the southeastern part of H2, whereas in eastern Salina the N-S fault crosses the overall low velocity zone from sea level to ~400 m b.s.l. The low velocity zones reflect the volcaniclastic deposits and reworked sediments filling the lowered side of the hanging wall of the main normal faults (Fig. 1c).

One of the oldest volcanic structures, Pizzo Capo is located (PCa in Fig. 4d) below the younger MtP (location in Fig. 4d) lavas and scoria successions and stands for the western volcanic roots of Salina strongly eroded and dismantled. At the north-western flank collapse of MtP, the Pollara Depression (PD and MtP in Fig. 4d) is partially filled by pumice fall and flow deposits, lacustrine, and fan-like deposits (Fig. 1c) covering the older lavas and overlapping the low velocity anomaly L1 (Fig. 5a). Away from MtP and below ~500 m b.s.l., L1 depicts a toe-like geometry, a feature often observed at the base of large landslides (Hungr et al., 2014). We propose that the L1 anomaly is due to lava debris resulting from the flank collapse of MtP (location in Fig. 4d) and the younger pyroclastic and sedimentary deposits filling the Pollara depression. Between MtP and MtFF (Fig. 4d), the low Vs anomaly L2 (Fig. 5a) overlaps

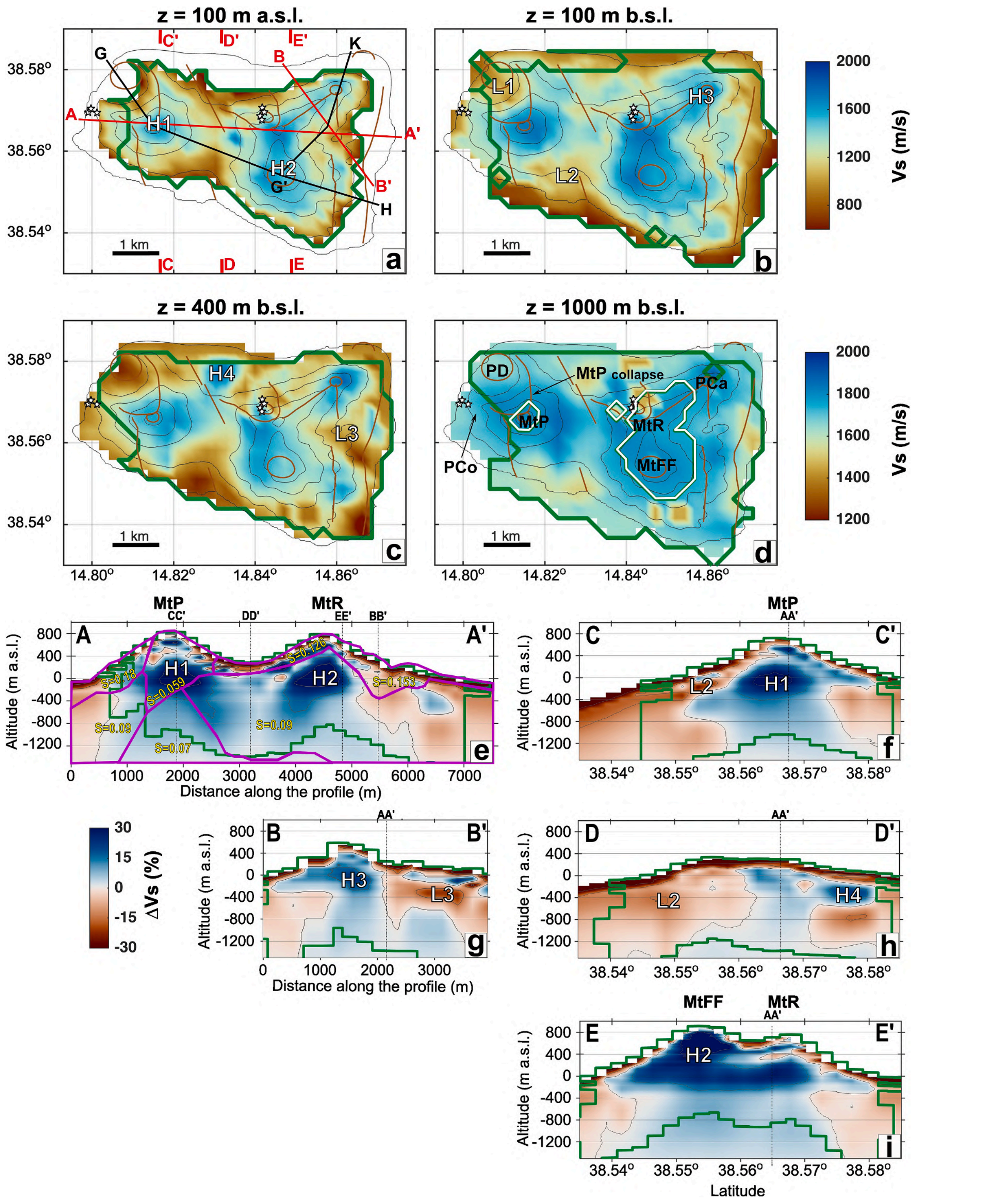

Fig. 4. 3D shear-wave velocity model from ambient noise tomography. **a - d.** Velocity maps at different depths. Black contours correspond to the topography (every 200 m). Faults, collapses and volcanic fissures are indicated as brown lines (Lucchi et al., 2013). Note that colour scales for velocity maps panels a-b and c-d are different to enhance low and high velocity patches. White contours from the spike-model (Rawlinson and Spakman, 2016; Figs. S3 and S4) in panel d indicate that below 1 km depth the velocity models are not resolved. **e - i.** Velocity anomaly (ΔVs) profiles (black contours at intervals of 0, + − 15% and + −30%) whose traces are shown in panel a as red lines. The thick green contour in each panel defines the resolution areas (supplementary material, Figs. S3 and S4). The magnetic susceptibility model from Cocchi et al. (2019) is reported in profile A-A' as magenta lines (numerical values indicate dimensionless magnetic susceptibility). (For interpretation of the references to colour in this figure legend, the reader is referred to the web version of this article.)

reworked, valley filling deposits (Fig. 1c). Such deposits, whose thickness is between 100-200 m, mainly consist of reworked scorias overlying early lava successions of MtP and MtFF (locations in Fig. 4d). The decrease of the velocity anomalies below 200 m b.s.l. depth imaged beneath the major volcanoes (MtP, MtFF and PCa, Fig. 4e-f, 4i, Fig. 5a-b; locations in Fig. 4d) is observed in other basaltic-andesitic volcanoes although at depths generally below 1000 m (Lesage et al., 2018). It is noteworthy that Salina is the emerging portion of a volcanic complex

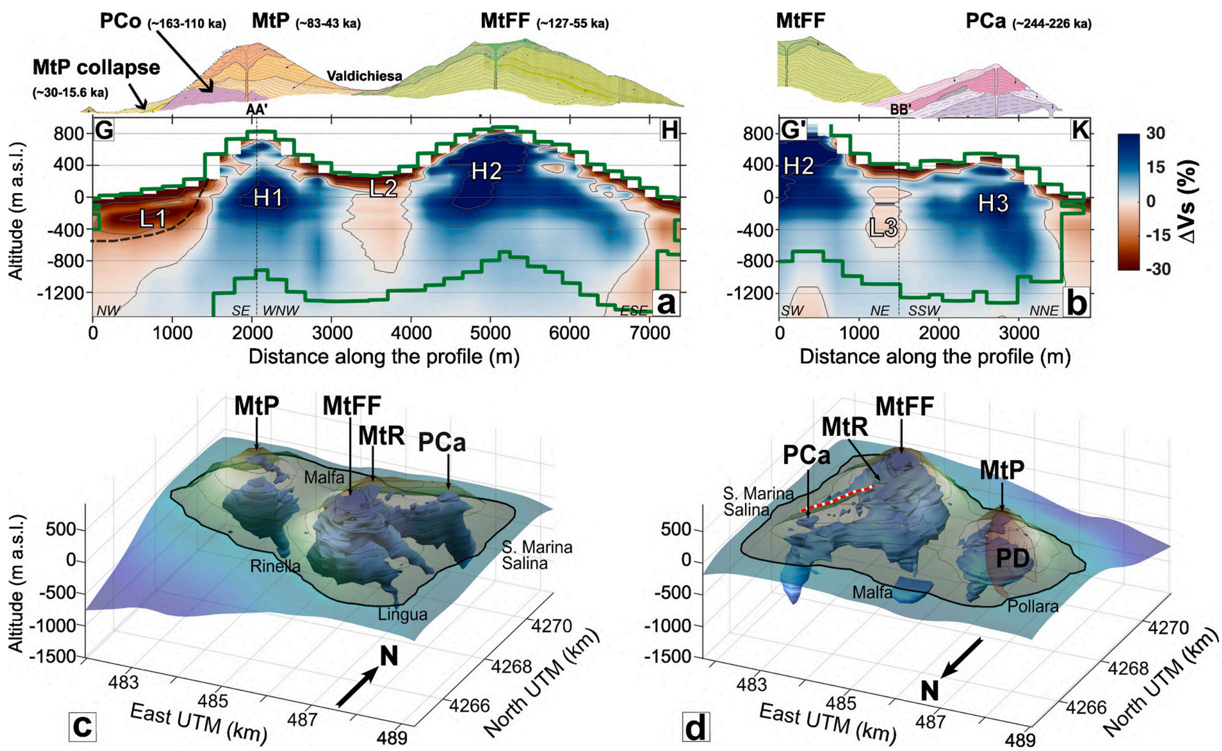

Fig. 5. Tomographic profiles from ambient noise tomography and corresponding geological sections from Lucchi et al. (2013). **a.** The G-H cross-section runs from the Pollara Depression through Monte dei Porri to Monte Fossa delle Felci and ends in the Lingua village. **b.** G'-K profile extends from MtFF to Pizzo Capo. Low and high velocity anomalies are labeled as shown in map view in Figs. 4 a-d. **c. and d.** 3D synoptic view of the tomographic model above 15% velocity anomalies from a south and a north perspective, respectively.

rising from ~1000 m b.s.l. and whose activity started under the sea level. At Salina, the submarine shelf edge is at depths between 120 m to 200 m b.s.l. (Casalbore et al., 2018), a depth range comparable to the maximum depth of 130 m b.s.l. reached by the sea level at 140 ka, 340 ka, and 430 ka (Bintanja et al., 2005). Consequently, the activity preceding the emersion of MtFF (147 ka) and PCa 244 ka) was largely submarine (Fig. 1c). We propose that the velocity variation, between 100 and 200 m b.s.l., marks the transition from a prevailing submerged, i.e. pillow lavas, to a subaerial activity, this latter dominated by the eruption of aʻā-type lava flows. Our conclusions agree with the model proposed by Cocchi et al. (2019) in which the transition from a prevailing widespread submarine activity to a subaerial, cone construction activity occurred at Salina.

The shallower dykes and conduits of Pizzo di Corvo (PCo in Fig. 4d) and the overlying MtP volcano are accountable for the high velocity anomaly H1 at depth (Fig. 4 a-d, profiles in Fig. 4e-f). This conclusion is supported by independent magnetic data (Fig. 11 in Cocchi et al., 2019) that show a high magnetic susceptibility (Fig. 4e, magenta contours). H1 and H2 velocity anomalies below MtP and MtFF-MtR (locations in Fig. 4d) can be interpreted as the sub-intrusive plug of the shallowest portion of the plumbing systems.

NE Salina is mainly covered by the MtFF, MtR, and PCa (locations in Fig. 4d) lavas and scorias (Fig. 4 and Fig. 5). The high velocity anomaly H3 (Fig. 4g and Fig. 5b) is associated with the sill-like intrusive body and overlying dyke system cutting the PCa lava flows and scoria successions (Lucchi et al., 2013). The thick accumulation of strombolian, loose scoria deposits in the valley between MtR and MtFF volcanoes (locations in Fig. 4d), overlaps a relatively low velocity anomaly L3 (Fig. 4 e-g, and Fig. 5b). This low anomaly could be associated with the hydrothermally altered rocks overlying the dyke-like high velocity body or, alternatively, with submarine volcaniclastic successions.

The high velocity anomaly (H4 in Fig. 4c and h) beneath the northeastern flank of MtP could be interpreted either as a thick sequence of lava flows related to the early MtP activity or, alternatively, as a sill-like body. Cocchi et al. (2019) found a low magnetic susceptibility region that overlaps H4 and allows us to propose that H4 represents a sill like body formed before the last magnetic inversion (~780 ka) and to exclude the lava flow sequence hypothesis, because the subaerial MtP lavas are younger than 70 ka.

The synoptic 3D view of the high velocity bodies beneath Salina (Fig. 5c-d) highlights the geometry of the main volcanoes. MtP, MtR, and MtFF plumbing systems form diapir-like structures from which apophyses propagate downward to the east (Fig. 5b). Diapir-like bodies at shallow crustal depths have been observed in shallow intrusions and interpreted to be formed by overlapped magma batches (Miller and Paterson, 1999; McCarthy et al., 2015). The plumbing system of PCa fissure consists of a subhorizontal dyke (Fig. 5c) whose eastward verging dyke-like apophysis propagates downward. At shallow depths, a small, sill-like body departs from the underlying subhorizontal dyke upward and stops just below the PCa crater (Fig. 5c).

The geometry of the Salina plumbing system indicates the control of the local tectonics on the magma propagation at depth during the early phases of volcanism (PCa volcanic fissure), and how the successive activity concentrates along central volcanoes. Following Cocchi et al. (2019), this evolution can be explained by a complex interaction of intrusions along pre-existing tectonic structures and dyke intersections. Comparable structural controls have been reported for Lipari and Vulcano, as documented by recent dense nodal seismic experiments and geological studies (Calò et al., 2023; Stumpp et al., 2025), suggesting a shared tectonic framework along the southernmost sector of the Aeolian arc.

It is noteworthy that, despite this common structural setting, the volcanism along the ATL differs from one island to another, reflecting the differences in the timing of volcanic activity: from older episodes (~240 ka) on Salina and Lipari to much younger activity (<8 ka) on Vulcano. Such temporal variations, among differences in local tectonic settings and lava compositions, likely control the distinct seismic velocity patterns and the development of volcanic centers across the islands.

Fluids further contribute to this variability, as highlighted by local earthquake tomography studies (Totaro et al., 2022), which indicate a stronger fluid-related imprint beneath Vulcano and the western sector of Lipari; in contrast, Salina shows comparatively limited evidence of active hydrothermal circulation.

The eastward dipping deeper sub-circular conduits below MtP, MtFF, and PCa suggest that the deep feeding system of these volcanoes is located at some depth eastward of the island. Our data coverage does not constrain the Salina velocity structure at depths larger than 1.5 km. An extended volcanic field characterizes Salina's eastern offshore (Favalli et al., 2005; Romagnoli et al., 2013). Therefore, as part of a wide volcanic area mainly located offshore in the Tyrrhenian Sea, and in light of our findings, we speculate that the deeper feeding system of Salina volcanoes would be located below this volcanic area. The above proposed off-axis location of the Salina deep feeding system is not an uncommon feature of volcanoes and has been recognized at Unzen (Japan; Umakoshi et al., 2001), Taupo (New Zealand; Hamling et al., 2016), and, in the Aeolian area, in the offshore of Calabria 60 km east of Salina, where a still degassing, Pleistocene submarine volcano with an inclined plumbing system has been recognized (Loreto et al., 2015).

6. Conclusions

Ambient Noise Tomography reveals important features that match the different volcanic stages to which the Salina Island underwent since its formation, including recent eruptions and volcanic episodes hidden by erosion processes. Our velocity model identifies the shallow structure of the plumbing system of the major volcanoes and fissures, the thickness of the main volcanic successions and reworked deposits, the heterogeneous structure of stratovolcanoes and volcanotectonic features including faults and flank collapses. Salina hosts a large variety of volcanic structures including (a) well-preserved central stratovolcanoes, eruptive fissures, deeply eroded and partly destroyed edifices, flank collapses, and (b) volcanic deposits related to effusive and explosive activity, from basaltic to andesitic strombolian scoria levels, to rhyolitic pumice falls and pyroclastic flow successions. In this framework, the deployment of dense portable cable-free nodal stations represents an essential approach to decipher the inner shallow structure of volcanoes. The long quiescent periods characterizing the Salina volcanism, coupled with the occurrence of seismic activity, thermal waters, and offshore hydrothermal emissions indicate that Salina is in a quiescent stage and a future reactivation of the magmatic system cannot be ruled out. Therefore, achieved results define a baseline image of the present-day crustal structure beneath Salina, that may be used to identify future variations on seismic properties which in turn could be associated with renewed volcanic activity and/or the development of inland hydrothermal manifestations.

CRediT authorship contribution statement

I. Granados-Chavarría: Writing – review & editing, Writing – original draft, Visualization, Validation, Software, Methodology, Investigation, Formal analysis, Data curation, Conceptualization. **F. Di Luccio:** Writing – review & editing, Writing – original draft, Visualization, Validation, Supervision, Resources, Project administration, Methodology, Investigation, Funding acquisition, Formal analysis, Data curation, Conceptualization. **M. Calò:** Writing – review & editing, Validation, Software, Methodology. **D. Famiani:** Writing – review & editing, Validation, Resources, Investigation. **M. Lupi:** Writing – review & editing, Validation, Resources, Investigation, Data curation. **M. Palano:** Writing – review & editing, Validation, Resources, Project administration, Investigation, Funding acquisition. **G. Ventura:** Writing – review & editing, Writing – original draft, Visualization, Validation, Investigation, Formal analysis.

Declaration of competing interest

We declare that we have no known competing financial interests or personal relationships that could have appeared to influence the work reported in this manuscript "Investigating the Seismic Structure of Shallow Magmatic Conduits: Insights from Salina Island (southern Italy)".

Acknowledgments

We thank L. Scognamiglio for taking part in the fieldwork, and personnel of Comuni di: Santa Marina, Malfa and Leni of Salina and Dr. Molino of Città Metropolitana di Messina for their support in the logistics. A special thanks to Mr. Elio Benenati, "Capo servizio della vigilanza della Riserva Naturale Orientata Le Montagne delle Felci e dei Porri" for his invaluable support during the experiment and his extensive knowledge of the island.

This work was supported by Project INGV Pianeta Dinamico 2023-2025 CAVEAT "The Central-southern Aeolian islands: Volcanism and tEArIng in the Tyrrhenian subduction system" funded by the Italian Ministry of University and Research. We thank the editor, the anonymous reviewer and Luca de Siena for their comments that contributed to improve the manuscript.

Appendix A. Supplementary data

Supplementary data to this article can be found online at https://doi.org/10.1016/j.jvolgeores.2026.108536.

Data availability

Empirical Green's functions and dispersion maps were calculated using matlab functions (MATLAB 2017a, The MathWorks, Inc., Natick, MA, United States). Empirical Green's functions of this study will be freely available at the repository "Salina Island cross-correlation functions" on the Zenodo platform (doi:https://doi.org/10.5281/zenodo.15375174). NDCP suite developed by the first author (Granados-Chavarría et al., 2019; https://github.com/IvanGCh/NDCP) is used to measure dispersion curves. Depth inversions were computed using the open-source Raylee code (Haney and Tsai, 2017; https://github.com/matt-haney/raylee_codes). Figures were produced using Adobe Creative Cloud Suite 6.6, MATLAB 2024a (The MathWorks, Inc., Natick, MA, United States) and Inkscape 1.4 (https://inkscape.org/).

References

Abe, Y., Ohkura, T., Shibutani, T., Hirahara, K., Yoshikawa, S., Inoue, H., 2017. Low-velocity zones in the crust beneath Aso caldera, Kyushu, Japan, derived from receiver function analyses. J. Geophys. Res. Solid Earth 122 (3), 2013–2033. https://doi.org/10.1002/2016JB013686.

Agius, M.R., Magrini, F., Diaferia, G., Kästle, E.D., Cammarano, F., Faccenna, C., Funiciello, F., Van der Meijde, M., 2022. Shear-velocity structure and dynamics beneath the Sicily Channel and surrounding regions of the Central Mediterranean inferred from seismic surface waves. Geochem. Geophys. Geosyst. 23, e2022GC010394. https://doi.org/10.1029/2022GC010394.

Albert, H., Muir, L., Pedrazzi, D., Gisbert, G., Bolós, X., Geyer, A., Aulinas, M., 2025. Unveiling the complexity of monogenetic volcanic fields: a petrological exploration of the Puig Jordà (Garrotxa Volcanic Field, Spain). J. Petrol. 66 (5), egaf032. https://doi.org/10.1093/petrology/egaf032.

Albino, F., Sigmundsson, F., 2014. Stress transfer between magma bodies: influence of intrusions prior to 2010 eruptions at Eyjafjallajökull volcano, Iceland. J. Geophys. Res. Solid Earth 119 (4), 2964–2975. https://doi.org/10.1002/2013JB010510.

Annen, C., Weinberg, R.F., Moyen, J.F., Cazabet, R., 2025. A complex system approach to magmatism. Nat. Rev. Earth Environ. https://doi.org/10.1038/s43017-025-00697-4.

Barmin, M.P., Ritzwoller, M.H., Levshin, A.L., 2001. A fast and reliable method for surface wave tomography. Pure Appl. Geophys. 158, 1351–1375. https://doi.org/10.1007/PL00001225.

Bedrosian, P.A., Peacock, J.R., Bowles-Martinez, E., Schultz, A., Hill, G.J., 2018. Crustal inheritance and a top-down control on arc magmatism at Mount St Helens. Nat. Geosci. 11 (11), 865–870. https://doi.org/10.1038/s41561-018-0217-2.

Bensen, G.D., Ritzwoller, M.H., Barmin, M.P., Levshin, A.L., Lin, F., Moschetti, M.P., Yang, Y., 2007. Processing seismic ambient noise data to obtain reliable broadband surface wave dispersion measurements. Geophys. J. Int. 169 (3), 1239–1260. https://doi.org/10.1111/j.1365-246x.2007.03374.x.

Billi, A., Cuffaro, M., Orecchio, B., Palano, M., Presti, D., Totaro, C., 2022. Retracing the Africa–Eurasia nascent convergent boundary in the western Mediterranean based on earthquake and GNSS data. Earth Planet. Sci. Lett. 601, 117906. https://doi.org/10.1016/j.epsl.2022.117906.

Bintanja, R., van de Wal, R., Oerlemans, J., 2005. Modelled atmospheric temperatures and global sea levels over the past million years. Nature 437, 125–128. https://doi.org/10.1038/nature03975.

Bortoluzzi, G., Ligi, M., Romagnoli, C., Cocchi, L., Casalbore, D., Sgroi, T., Cuffaro, M., Caratori Tontini, F., D'Oriano, F., Ferrante, V., 2010. Interactions between volcanism and tectonics in the western Aeolian sector, southern Tyrrhenian Sea. Geophys. J. Int. 183 (1), 64–78. https://doi.org/10.1111/j.1365-246X.2010.04729.x.

Bushenkova, N., Koulakov, I., Senyukov, S., Gordeev, E.I., Huang, H.-H., El Khrepy, S., Al Arifi, N., 2019. Tomographic images of magma chambers beneath the Avacha and Koryaksky volcanoes in Kamchatka. J. Geophys. Res. Solid Earth 124, 9694–9713. https://doi.org/10.1029/2019JB017952.

Cabrera-Pérez, I., Soubestre, J., D'Auria, L., Martínez-van-Dorth, D., Ledo, J., Piña-Varas, P., Cervigón-Tomico, G., Padilla, D., G., Barrancos, J., and Pérez, N. M., 2023. Ambient noise tomography of Gran Canaria island (Canary Islands) for geothermal exploration. Geothermics 108, 102609. https://doi.org/10.1016/j.geothermics.2022.102609.

Calò, M., Parisi, L., Luzio, D., 2013. Lithospheric P- and S-wave velocity models of the Sicilian area using WAM tomography: procedure and assessments. Geophys. J. Int. 195 (1), 625–649. https://doi.org/10.1093/gji/ggt252.

Calò, M., Di Luccio, F., Persaud, P., Ventura, G., 2023. Ambient noise tomography of the Lipari Volcanic Island (Southern Italy) from a Dense Nodal Array. Geophys. Res. Lett. 50, e2022GL101022. https://doi.org/10.1029/2022GL101022.

Canón-Tapia, E., 2016. Reappraisal of the significance of volcanic fields. J. Volcanol. Geotherm. Res. 310, 26–38. https://doi.org/10.1016/j.jvolgeores.2015.11.010.

Casalbore, D., Romagnoli, C., Adami, C., Bosman, A., Falese, F., Ricchi, A., Chiocci, F.L., 2018. Submarine depositional terraces at Salina Island (Southern Tyrrhenian Sea) and Implications on the late-quaternary evolution of the insular shelf. Geosciences 8 (1), 20. https://doi.org/10.3390/geosciences8010020.

Chambers, E.L., Harmon, N., Rychert, C.A., Keir, D., 2021. Variations in melt emplacement beneath the northern East African Rift from radial anisotropy. Earth Planet. Sci. Lett. 573, 117150. https://doi.org/10.1016/j.epsl.2021.117150.

Cocchi, L., De Ritis, R., Casalbore, D., Romagnoli, C., Lucchi, F., Tranne, C.A., Ventura, G., 2019. Seamount-volcanic island transition and evolution from fissural to central activity inferred by the magnetic modeling of Salina Island (Tyrrhenian Sea). J. Geophys. Res. Solid Earth 124, 4323–4342. https://doi.org/10.1029/2018JB017113.

De Astis, G., Ventura, G., Vilardo, G., 2003. Geodynamic significance of the Aeolian volcanism (Southern Tyrrhenian Sea, Italy) in light of structural, seismological, and geochemical data. Tectonics 22 (4), 1040. https://doi.org/10.1029/2003TC001506.

De Siena, L., Sammarco, C., Cornwell, D.G., La Rocca, M., Bianco, F., Zaccarelli, L., Nakahara, H., 2018. Ambient seismic noise image of the structurally controlled heat and fluid feeder pathway at Campi Flegrei caldera. Geophys. Res. Lett. 45, 6428–6436. https://doi.org/10.1029/2018GL078817.

DeVitre, C.L., Gazel, E., Allison, C.M., Soto, G., Madrigal, P., Alvarado, G.E., Lücke, O.H., 2019. Multi-stage chaotic magma mixing at Turrialba volcano. J. Volcanol. Geotherm. Res. 381, 330–346. https://doi.org/10.1016/j.jvolgeores.2019.06.011.

Esquivel-Mendiola, L.I., Calò, M., Iglesias, A., Tago, J., Macías, J.L., 2024. Seismic velocity structure of Popocatépetl volcano, Mexico from diffusive fields. J. Volcanol. Geotherm. Res. 449, 108071. https://doi.org/10.1016/j.jvolgeores.2024.108071.

Favalli, M., Karatson, D., Mazzuoli, R., Pareschi, M.T., Ventura, G., 2005. Volcanic geomorphology and tectonics of the Aeolian Archipelago (Southern Italy) based on integrated DEM data. Bull. Volcanol. https://doi.org/10.1007/s00445-005-0429-3.

Finetti, I., Del Ben, A., 1986. Geophysical study of the Tyrrhenian opening. Boll. Geofis. Teor. Appl. 110, 75–156.

Granados-Chavarría, I., Calò, M., Ramos, V., 2019. Noisy dispersion curve picking (NDCP): a Matlab package for group velocity dispersion picking of seismic surface waves. Comput. Geosci. 133, 104315. https://doi.org/10.1016/j.cageo.2019.104315.

Granados-Chavarría, I., Calò, M., Figueroa-Soto, Á., Jousset, P., 2022. Seismic imaging of the magmatic plumbing system and geothermal reservoir of the Los Humeros caldera (Mexico) using anisotropic shear wave models. J. Volcanol. Geotherm. Res. 421, 107441. https://doi.org/10.1016/j.jvolgeores.2021.107441.

Hamling, I.J., Hreinsdóttir, S., Bannister, S., Palmer, N., 2016. Off-axis magmatism along a subaerial back-arc rift: observations from the Taupo Volcanic Zone, New Zealand. Sci. Adv. 2, e1600288. https://doi.org/10.1126/sciadv.1600288.

Haney, M.M., Tsai, V.C., 2017. Perturbational and non-perturbational inversion of Rayleigh-wave velocities. Geophysics 82 (3), F15–F28. https://doi.org/10.1190/geo2016-0397.1.

Hansen, P., 2001. The L-curve and its use in the numerical treatment of inverse problems. In: Johnston, P. (Ed.), Advances in Computational Bioengineering. WIT Press, Southampton U.K.

Heath, B.A., Hooft, E.E.E., Toomey, D.R., Papazachos, C.B., Nomikou, P., Paulatto, M., et al., 2019. Tectonism and its relation to magmatism around Santorini Volcano from upper crustal P wave velocity. J. Geophys. Res. Solid Earth 124 (10), 10610–10629. https://doi.org/10.1029/2019jb017699.

Hungr, O., Leroueil, S., Picarelli, L., 2014. The Varnes classification of landslide types, an update. Landslides 11, 167–194. https://doi.org/10.1007/s10346-013-0436-y.

Italiano, F., Caruso, C., 2011. Detection of fresh and thermal waters over an island with extinct volcanism: the island of Salina (Aeolian arc, Italy). Proc. Earth Planet. Sci. 4, 39–49. https://doi.org/10.1016/j.proeps.2011.11.005, 2-s2.0-84858261065.

Jiwani-Brown, E.A., Planès, T., Pacheco, J.F., Mora, M.M., Lupi, M., 2022. Magmatic and tectonic domains of central Costa Rica and the Irazú-Turrialba volcanic complex revealed by ambient noise tomography. J. Geophys. Res. Solid Earth 127 (11). https://doi.org/10.1029/2022JB024575.

Keller, J., 1980. The island of Salina. Rend. Soc. Ital. Mineral. Petrol. 36, 489–524.

Klein, F.W., 1982. Patterns of historical eruptions at Hawaiian volcanoes (1982). J. Volcanol. Geotherm. Res. 12, 1–35. https://doi.org/10.1016/0377-0273(82)90002-6.

Lesage, P., Heap, M., Kushnir, A., 2018. A generic model for the shallow velocity structure of volcanoes. J. Volcanol. Geotherm. Res. https://doi.org/10.1016/j.jvolgeores.2018.03.003.

Li, Y., Weng, A., Xu, W., Zou, Z., Tang, Y., Zhou, Z., Li, S., Zhang, Y., Ventura, G., 2021. The trans-lithospheric magma plumbing system of intraplate volcanoes as revealed by electrical resistivity imaging. Geology 49. https://doi.org/10.1130/G49032.1.

Loreto, M.F., Pepe, F., De Ritis, R., Ventura, G., Ferrante, V., Speranza, F., Tomini, I., Sacchi, M., 2015. Geophysical investigation of pleistocene volcanism and tectonics offshore Capo Vaticano (Calabria, southeastern Tyrrhenian Sea). J. Geodyn. 90, 71–86. https://doi.org/10.1016/j.jog.2015.07.005.

Lucchi, F., Peccerillo, A., Keller, J., Tranne, C.A., Rossi, P.L., 2013. The Aeolian Islands volcanoes. Geol. Soc. Lond. Mem. 37, 155–211. https://doi.org/10.1144/M37.9.

Madonia, P., Cangemi, M., Colajanni, M., Winkler, A., 2022. Atmospheric concentration of CO2 and PM2.5 at Salina, stromboli, and Vulcano Islands (Italy): how anthropogenic sources, ordinary volcanic activity and unrests affect air quality. Int. J. Environ. Res. Public Health 19, 4833. https://doi.org/10.3390/ijerph19084833.

McCarthy, W., Petronis, M.S., Reavy, R.J., Stevenson, C.T., 2015. Distinguishing diapirs from inflated plutons: an integrated rock magnetic fabric and structural study on the Roundstone Pluton, western Ireland. Geol. Soc. J.172, 550–565. https://doi.org/10.1144/jgs2014-067.

McVey, B.G., Hooft, E.E.E., Heath, B.A., Toomey, D.R., Paulatto, M., Morgan, J.V., et al., 2020. Magma accumulation beneath Santorini volcano, Greece, from P-wave tomography. Geology 48 (3), 231–235. https://doi.org/10.1130/g47127.1.

Menke, W., 1989. Geophysical Data Analysis: Discrete Inverse Theory. Academic, San Diego, CA.

Miller, R.B., Paterson, S.R., 1999. In defense of magmatic diapirs. J. Struct. Geol. 21, 1161–1173. https://doi.org/10.1016/s0191-8141(99)00033-4.

Muller, C., Alvarado, Guillermo E., Angarita, M., Avard, G., 2024. Spatiotemporal deformation and activity distribution of Irazú and Turrialba volcanoes, Costa Rica: are these volcanoes interconnected? J. Volcanol. Geotherm. Res. 449, 108052. https://doi.org/10.1016/j.jvolgeores.2024.108052.

Neri, G., Caccamo, D., Cocina, O., Montalto, A., 1996. Geodynamic implications of earthquake data in the southern Tyrrhenian Sea. Tectonophysics 258 (1–4), 233–249. https://doi.org/10.1016/0040-1951(95)00202-2.

Patanè, D., Barberi, G., Cocina, O., De Gori, P., Chiarabba, C., 2006. Time-resolved seismic tomography detects magma intrusions at Mount Etna. Science 313 (5788), 821–823. https://doi.org/10.1126/science.1127724.

Paulatto, M., Hooft, E.E.E., Chrapkiewicz, K., Heath, B., Toomey, D.R., Morgan, J.V., 2022. Advances in seismic imaging of magma and crystal mush. Front. Earth Sci. 10, 970131. https://doi.org/10.3389/feart.2022.970131.

Przeor, M., D'Auria, L., Pepe, S., Tizzani, P., Cabrera-Pérez, I., 2022. Elastic interaction between Mauna Loa and Kīlauea evidenced by independent component analysis. Sci. Rep. 12 (1), 1–13. https://doi.org/10.1038/s41598-022-24308-0.

Rawlinson, N., Spakman, W., 2016. On the use of sensitivity tests in seismic tomography. Geophys. J. Int. 205, 1221–1243. https://doi.org/10.1093/gji/ggw084.

Romagnoli, C., Calanchi, N., Gabbianelli, G., Lanzafame, G., Rossi, P.L., 1989. Contributi delle ricerche di geologia marina alla caratterizzazione morfostrutturale ed evolutiva dei complessi vulcanici di Salina, Lipari e Vulcano (Is. Eolie). Bollettino GNV 1989, 971–978.

Romagnoli, C., Casalbore, D., Bortoluzzi, G., Bosman, A., Chiocci, F., D'Oriano, L., Gamberi, F., Ligi, M., Marani, M., 2013. Bathy-morphological setting of the Aeolian Islands. Geol. Soc. Lond. Mem. 37, 27–36. https://doi.org/10.1144/M37.4.

Rosenbaum, G., Lister, G.S., 2004. Neogene and quaternary rollback evolution of the Tyrrhenian Sea, the Apennines and the Sicilian maghrebides. Tectonics 23, TC1013. https://doi.org/10.1029/2003TC001518.

Schimmel, M., 1999. Phase cross-correlations: Design, comparisons, and applications. Bull. Seismol. Soc. Am. 89 (5), 1366–1378. https://doi.org/10.1785/BSSA0890051366.

Shapiro, N.M., Campillo, M., 2004. Emergence of broadband Rayleigh waves from correlations of the ambient seismic noise. Geophys. Res. Lett. 31, L07614. https://doi.org/10.1029/2004GL019491.

Smith, I.E.M., Németh, K., 2017. Source to surface model of monogenetic volcanism: a critical review. Geol. Soc. Lond. Spec. Publ. 446 (1), 1–28. https://doi.org/10.1144/SP446.14.

Spica, Z., Perton, M., Legrand, D., 2017. Anatomy of the Colima volcano magmatic system, Mexico. Earth Planet. Sci. Lett. 459, 1–13. https://doi.org/10.1016/j.epsl.2016.11.010.

Stumpp, D.S., Cabrera-Pérez, I., Savard, G., Ricci, T., Palano, M., Alparone, S., Ursino, A., Sparacino, F., Finizola, A., Muñoz-Burbano, F., Reyes Hardy, M.P., Ruch, J., Bonadonna, C., Lupi, M., 2025. Neural network nodal ambient noise tomography of a transient plumbing system under unrest, Vulcano, Italy. Nat. Commun. 16, 7687. https://doi.org/10.1038/s41467-025-62846-z.

Totaro, C., Aloisi, M., Ferlito, C., Orecchio, B., Presti, D., Scolaro, S., 2022. New insights on the active degassing system of the Lipari–Vulcano complex (South Italy) inferred from Local Earthquake Tomography. Sci. Rep. 12, 18867. https://doi.org/10.1038/s41598-022-21921-x.

Umakoshi, K., Shimizu, H., Matsuwo, N., 2001. Volcano-tectonic seismicity at Unzen Volcano, Japan, 1985–1999. J. Volcanol. Geotherm. Res. 112, 117–131. https://doi.org/10.1016/S0377-0273(01)00238-4.

Ventura, G., Vilardo, G., Milano, G., and Pino, N. A. (1999). Relationships among crustal structure, volcanism and strike–slip tectonics in the Lipari–Vulcano Volcanic Complex (Aeolian Islands, Southern Tyrrhenian Sea, Italy). Phys. Earth Planet. Inter. 116, 31–52. doi:https://doi.org/10.1016/S0031-9201(99)00117-X.